

Ultrafast Faraday spectroscopy in magnetic semiconductor quantum structures

J. J. Baumberg, S. A. Crooker, and D. D. Awschalom

Department of Physics, University of California, Santa Barbara, California 93106

N. Samarth

Department of Physics, The Pennsylvania State University, University Park, Pennsylvania 16802

H. Luo and J. K. Furdyna

Department of Physics, University of Notre Dame, Notre Dame, Indiana 46556

(Received 7 February 1994; revised manuscript received 2 May 1994)

We use an optical probe of magnetization to explore the evolution of carrier-spin scattering and magnetic dynamics in quantum-confined geometries. II-VI magnetic heterostructures are studied using femtosecond-resolved Faraday rotation and exhibit both phase (~ 1 ps) and spin scattering (~ 6 ps) in concert with a field-tunable terahertz quantum beating of the total carrier spin. Spin-flip processes experienced by photoexcited carriers as they tunnel through nanometer-thick magnetic barriers produce a magnetic perturbation strongly sensitive to the initial magnetic state and the spin orientation of the carriers. Once these carriers have recombined (~ 70 ps), the magnetic ions relax through completely different channels of significantly slower decay rate (100 ps–10 ns). The relaxation characteristics are found to be substantially influenced by exchange coupling between adjacent magnetic ions at low temperatures ($T < 13$ K). These low-dimensional magnetic systems yield a rich array of spin phenomena absent in traditional semiconductor heterostructures.

I. INTRODUCTION

A substantial portion of current research in condensed-matter physics is directed toward understanding various manifestations of spin-dependent phenomena (e.g., “giant” magnetoresistance, Kondo scattering, heavy fermions, and superconductivity). In the majority of these, interplay between two interacting spin systems provides the physical basis for the properties. Frequently this is realized by using an ensemble of embedded magnetic spins to control the behavior of a sea of carriers. Studies of the dynamic component of these interactions are rarely attempted despite the more sophisticated information revealed as compared to macroscopic static measurements. In fact, very few direct measurements of the temporal response of any magnetic systems exist, and most current understanding is gleaned from the spectral domain. The need for experimental data is fueled by an accelerating interest in nanofabricated magnets which possess extremely small magnetizations but can yield unexpected dynamics.

An ideal prototype system in which to study these spin interactions is a magnetic semiconductor, because it combines the prospect of adjusting scattering rates, carrier densities, and micromagnetic behavior, with the power and flexibility of optical interrogation. In diluted magnetic semiconductors (DMS's), there is an extremely strong spin-sensitive $sp-d$ exchange interaction between mobile carriers and the embedded magnetic ions, which amplifies many fold the g factors of the electrons and holes.¹ The present availability of DMS heterostructures in specially tailored geometries enables an investigation of detailed spin processes.² Such “spin-engineered” sam-

ples allow the simultaneous control of both the electronic carrier wave functions (which furnish carriers to be scattered), and the magnetic medium they encounter. Magnetically doped II-VI alloys have been studied comprehensively using static methods, although conventional time-resolved spectroscopies have not proved entirely satisfactory probes of the magnetic behavior. In this paper, we describe the use of a recently developed time-resolved Faraday rotation technique, which we show is appropriate for the study of spin dynamics in such quantum structures. By exploring both charge-carrier and magnetic-ion dynamics, we demonstrate the unusual properties of this class of materials.

Sensitive magnetic measurements on a variety of DMS structures exhibit the critical influence of the interaction geometry, and portray the characteristic static properties of exceedingly thin magnetic alloys. Time-resolved data from a particular structure consisting of quantum wells which are coupled by a thin magnetic tunneling barrier uncover both spin scattering (~ 6 ps) and phase scattering (~ 1 ps) of photoinjected carriers. As a magnetic field is applied, an ultra-long-lived magnetic “imprint” is generated by the carriers which subsequently recombine (~ 70 ps), leaving behind a highly perturbed magnetic spin system. In contrast to conventional semiconductor heterostructures, complete relaxation of the sample requires several microseconds. Using selective spin excitation of the dominant heavy-hole excitons reveals an unexpected carrier-orientation dependence of the excitation and recovery of the magnetic ions. This is tentatively ascribed to the capability of tunneling carriers in overcoming large superexchange forces between neighboring magnetic cations.

The manuscript is organized as follows: Section II details the sample design and basic optical properties, while Sec. III describes the experiments which verify their magnetization through ultrasensitive Faraday rotation. Section IV A describes the technique used to extend these measurements into the time domain, and the results are presented in Secs. IV B and IV C. A discussion of their interpretation fills Sec. V, after which we summarize our main results.

II. SAMPLE CHARACTERISTICS

Advances in molecular-beam epitaxy now enable the growth of high quality II-VI semiconductor heterostructures for use in optical studies. The introduction of magnetic ions allows further engineering of the magnetic properties of these structures. Work detailed in this publication utilizes $\text{Zn}_{1-x}\text{Mn}_x\text{Se}$, which features one of the largest *sp-d* exchange coupling strengths for this class of materials and incorporates Mn^{2+} ions that behave predominantly as $S = \frac{5}{2}$ paramagnets above $T \sim 10$ K. In addition, the (Zn,Mn,Cd)Se alloy system exhibits a nonlinear dependence of the electronic band gap on magnetic concentration that provides flexibility in fabricating both magnetic quantum wells and magnetic tunneling barriers. Two such heterostructure designs (termed spin superlattices and magnetically coupled double quantum wells) were grown on (100) GaAs insulating substrates with a 0.6–1- μm ZnSe buffer that relaxes the strain mismatch from the GaAs interface. In addition, the samples are protectively capped with a further 100–200 nm of ZnSe, so that the thin sandwich of alloy layers is coherently strained to match the ZnSe lattice.

The first sequence of structures, known as “spin superlattices” (SSL’s) consists of ten periods of 100-Å-thick alternating layers of ZnSe and $\text{Zn}_{0.92}\text{Mn}_{0.08}\text{Se}$. As grown, the electronic potentials for these two compositions almost coincide with a shallow quantum well for both electrons and holes in the magnetic alloy [Fig. 1(a)]. Application of a magnetic field Zeeman splits the band gap in the ZnMnSe, rapidly deepening the quantum well for spin-down carriers, while reducing the confinement of spin-up carriers. Above modest fields, $B_{\text{SSL}} \sim 0.50$ T, both spin-up electrons and holes are ejected from the magnetic quantum-well region and spatially relocate to the nonmagnetic ZnSe layers, resulting in a periodic array of alternating carrier spins after which the structure is named. It is the large spatial overlap of the electronic wave function and the magnetic ions in the SSL that gives rise to Zeeman splittings reaching 10 meV/T, as seen in low-temperature magnetoabsorption data [Fig. 1(b)]. This is in contrast to nonmagnetic heterostructures, where Zeeman splittings are on the order of 0.1 meV/T and the second set of structures described below. In addition to clear, field-tunable spin-up and spin-down exciton absorption peaks (assigned via circular polarization analysis as described below), strong magnetically inactive excitonic features associated with the ZnSe buffer and cap layers are visible at 2.800 and 2.805 eV. The field suppression of the weak, zero-field peak at 2.813 eV is tentatively ascribed to a “quasibound” resonance³

in the ZnSe barrier layers which evolves into the spin-up confined state once the applied field exceeds B_{SSL} .

A second set of systems involves magnetically coupled double quantum wells (MCDQW’s). In marked contrast, these structures exhibit only a fraction of the SSL *g* factor, since the carrier and ion wave functions overlap only when the carriers tunnel through a thin magnetic barrier. This $\text{Zn}_{0.76}\text{Mn}_{0.24}\text{Se}$ layer of thickness $L_B = 12, 24$, or 32 Å, magnetically modulates the coupling between two adjacent 40-Å nonmagnetic $\text{Zn}_{0.77}\text{Cd}_{0.23}\text{Se}$ quantum wells whose alloy composition ensures deep confinement potentials [Fig. 2(a)]. The coupling between the two wells gives rise to separate symmetric and antisymmetric double-quantum-well exciton states whose splitting is estimated to range from ~ 5 ($L_B = 32$ Å) to ~ 30 meV ($L_B = 12$ Å). In no case are there any marked absorption resonances

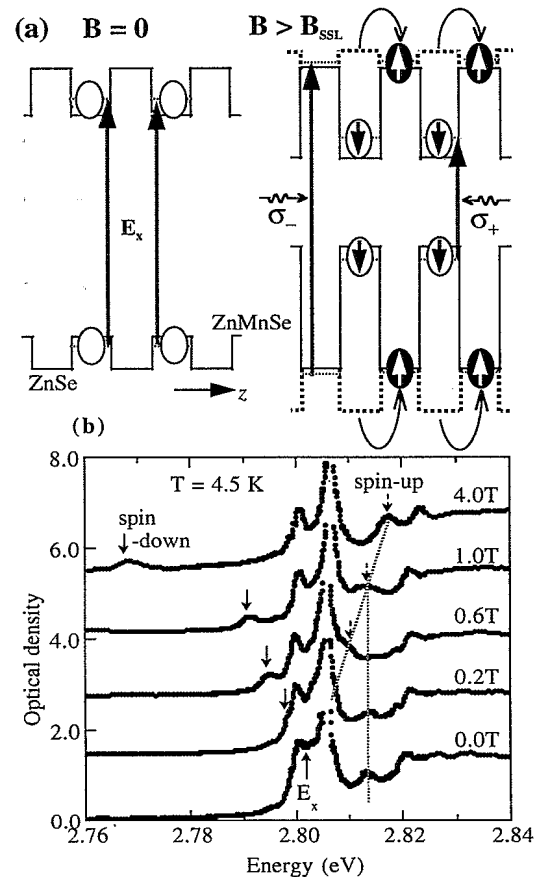


FIG. 1. (a) Conduction- and valence-band potentials at $k=0$ along the z axis of the spin superlattice (SSL) structure showing weak carrier confinement in the $\text{Zn}_{0.92}\text{Mn}_{0.08}\text{Se}$ magnetic quantum wells (shaded) at zero field. The lowest electron and heavy-hole states are shown together with the exciton transition energy E_x . When the magnetic field exceeds B_{SSL} , the spin-up carriers spatially transfer into the ZnSe barrier layers. The spin-split excitons interact with opposite circular polarizations of light, as shown. (b) The magnetoabsorption in fields up to $B = 4$ T showing the Zeeman splitting of spin-up (dashed arrows) and spin-down excitons (solid arrows). The zero-field exciton energy E_x coincides with excitonic features from the ZnSe buffer and cap. Other features are discussed in the text.

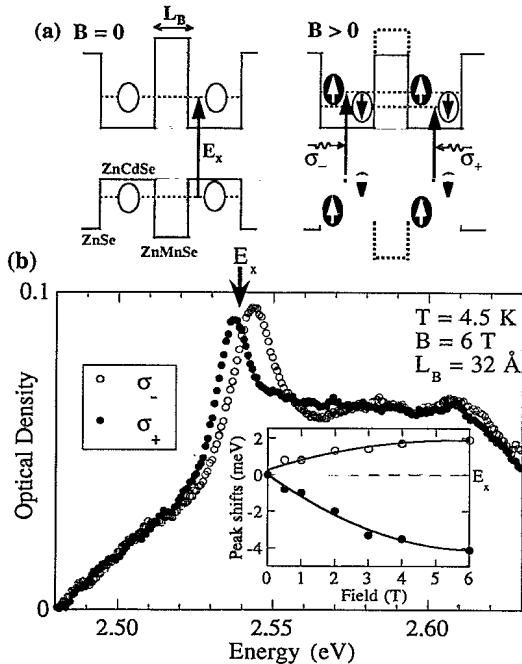


FIG. 2. (a) Conduction- and valence-band potentials at $k=0$ along the z axis of the magnetically coupled double-quantum-well (MCDQW) structure. Zeeman splitting due to the magnetic barrier (shaded) in magnetic field leads to spin-split excitons, each coupled to one circular polarization of light. Only the lower-energy, symmetric, heavy-hole, coupled-DQW exciton is apparent. (b) Polarization-resolved magneto-absorption identifies spin-down (σ_+) and spin-up (σ_-) excitons. Inset: Field-induced energy shifts of the exciton peaks at $T=4.5$ K.

corresponding to the higher-energy antisymmetric exciton, which is hence assumed to play little role in the experiments. As a magnetic field is applied, the tunneling dynamics become distinct for the two spin populations, and the lowest-energy symmetric superposition state is further Zeeman split [Fig. 2(b)]. The energy splitting reflects a spatial average over the Bohr orbit of spin-dependent exchange interactions between carriers and Mn^{2+} ions whose spins align progressively as the magnetic field increases. This splitting closely tracks the magnetization of the ultrathin layers, thus seen to act paramagnetically and follow the expected Brillouin dependence¹ on $\mu B/kT$ [inset, Fig. 2(b)].

Layer thicknesses and magnetic concentrations in these samples are determined from reflection-high-energy electron-diffraction (RHEED), x-ray, TEM, and low-temperature photoluminescence (PL) data along with associated $1\text{-}\mu\text{m}$ -thick epilayer samples of the same Mn^{2+} dilution grown for magnetic characterization purposes. In order to optically probe these quantum structures in transmission, the GaAs substrate must be etched away since its absorption coefficient is $\sim 10^4\text{ cm}^{-1}$ in the energy range of interest. Initial mechanical polishing down to $50\text{ }\mu\text{m}$ is accomplished by epoxying the ZnSe structure directly onto nonbirefringent $200\text{-}\mu\text{m}$ -thick fused silica plates and using standard polishing abrasives. The subsequent chemical etchant is a 1:20 solution of $\text{NH}_4\text{OH}:\text{H}_2\text{O}_2$, providing a GaAs etch rate of $5\text{ }\mu\text{m}/\text{min}$.

This is sufficiently slow that it can be abruptly terminated before the ZnSe buffer layer is etched down to the deeper quantum structures (no II-VI etch stop is known).

Throughout this work, the samples are held in the Faraday configuration with the applied magnetic field parallel to the incident light, and also to the growth axis of the heterostructures. The selection rules for absorption and emission of photons are then particularly useful since each opposing circular polarization of light (σ_{\pm}) excites and probes a particular sense of exciton spin, down or up, respectively.¹ This spin-dependent optical coupling also provides the basis for the Faraday rotation measurements presented below since the circular birefringence ($\eta_+ \neq \eta_-$) introduced when a magnetic field is applied rotates the plane of linearly polarized incident probe light.

III. STATIC MAGNETIZATION

To demonstrate the sensitivity and both spatial and spectral selectivity of the Faraday rotation techniques, we first present dc measurements of the magnetization in these ultrathin structures. With nanometer-thick magnetic layers, however, special techniques are needed to isolate the very small Faraday rotations θ_F produced by magnetically coupled DQW heterostructures. Figure 3 shows the balanced “optical bridge” arrangement employed, which uses a Glan-laser prism to divide light emerging from the sample into two orthogonal polarizations. These are separately focused onto matched Si photodiodes whose photocurrents are amplified and subtracted yielding an output signal, $D \propto \cos^2\theta_t - \sin^2\theta_t$, when the transmitted probe polarization is at an angle $\theta_t = \theta_{\lambda/2} + \theta_F$ to the prism axes. If $\theta_t = 45^\circ$ (as set by adjusting the half-wave plate $\theta_{\lambda/2}$) the bridge is balanced, and fluctuations in probe intensity are canceled in the output so that small additional rotations in polarization can be distinguished above the optical noise floor. This arrangement is sensitive to rotations of <1 arcsec when optimally aligned, limited by amplitude and polarization

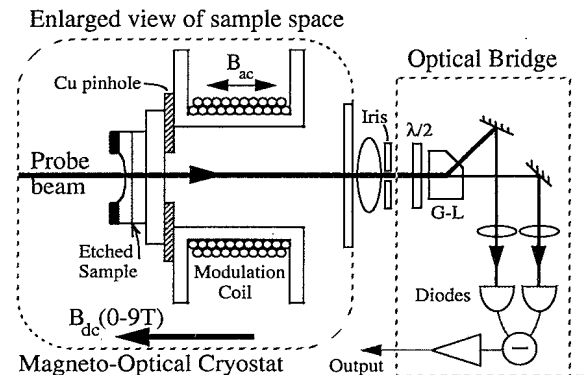


FIG. 3. Schematic diagram of the differential Faraday rotation apparatus showing the etched sample fixed to the miniature modulation coil. The emerging light is polarization analyzed in an optical bridge. [$\lambda/2$ =half-wave plate rotatable by computer control, at $\theta_{\lambda/2}$ to the Glan-laser (G-L) prism which separates orthogonal linear polarizations.]

noise on the probe laser beam (dominant in the data reported here) and electronic noise in the detection. The ultimate rotation sensitivity is nominally constrained by the shot noise of the light intensities used, which currently contributes 10% to the noise (for probe powers $\sim 3 \mu\text{W}$). The samples are mounted in a strain-free geometry on copper pinholes ($d \sim 300 \mu\text{m}$) to ensure that only light transmitted through the sample reaches the detectors. All experiments are carried out in a variable-temperature magneto-optic cryostat capable of magnetic fields up to 9 T at temperatures between 1.7 and 300 K. Once magnetic fields are applied, residual Faraday rotations which appear from the majority of optical components mask that of the sample due to the $\sim 10^7$ ratio of thicknesses. To overcome this signal contamination, a modulation scheme is adopted which uses a miniature coil directly behind the sample to provide an additional oscillatory magnetic field of amplitude $\sim 5 \text{ mT}$.⁴ Phase-sensitive electronics separates out the component of Faraday rotation ($\partial D / \partial B$) oscillating at this frequency (105 Hz). To provide a measure of the differential Faraday rotation (DFR), the total intensity reaching the detectors (I) is recorded for normalization; thus when balanced

$$\text{DFR} = \frac{\partial D}{\partial B} / 2I = \sin(2\theta_t) \frac{\partial \theta_t}{\partial B} \equiv \frac{\partial \theta_F}{\partial B} \quad (1)$$

A computer-controlled broadband, zero-order half-wave plate rotates the probe polarization after the sample and keeps the optical bridge balanced as the static magnetic field is ramped. The probe beam derived from the pulsed laser source discussed below can be wavelength tuned across the exciton resonances displayed in Figs. 1(b) and 2(b) and is attenuated below $10 \mu\text{W}$ in order to minimize saturation effects (Sec. IV B). Less than 10% of it is absorbed in the MCDQW samples when focused through a $100\text{-}\mu\text{m}$ spot, thus eliciting negligible changes in ellipticity as verified by the $>99\%$ linearly-polarized nature of the emerging beam.

Spectral DFR measurements in Fig. 4(a) taken on the thinnest magnetic layer at $T=4.5 \text{ K}$ and $B=0 \text{ T}$ exhibit a peak clearly coinciding with the exciton absorption energy. The form of this resonance can be derived from a Kramers-Krönig (KK) transformation of the magnetoabsorption. For a sample length L_{eff} , and refractive indices η_{\pm} , corresponding to the two circular polarizations σ_{\pm} , we have, for the frequency-dependent Faraday rotation,

$$\theta_F(\omega) = \frac{\omega L_{\text{eff}}}{2c} \{ \eta_+ - \eta_- \}, \quad (2)$$

thus

$$\text{DFR}(\omega) = \frac{\omega L_{\text{eff}}}{2c} \frac{\partial}{\partial B} \{ \eta_+ - \eta_- \} \quad (3)$$

$$\begin{aligned} &= \frac{\omega L_{\text{eff}}}{2\pi} P \int_0^\infty \frac{dv}{v^2 - \omega^2} \frac{\partial}{\partial B} \{ \alpha_+(v) - \alpha_-(v) \} \\ &\cong \frac{\omega L_{\text{eff}}}{2\pi} \frac{\mu_B g_{\text{eff}}}{\hbar} P \int_0^\infty \frac{dv}{v^2 - \omega^2} \frac{\partial \alpha}{\partial B} \Big|_{B=0} \end{aligned}$$

using the absorption dichroism $\alpha_+(v) - \alpha_-(v) = \partial \alpha /$

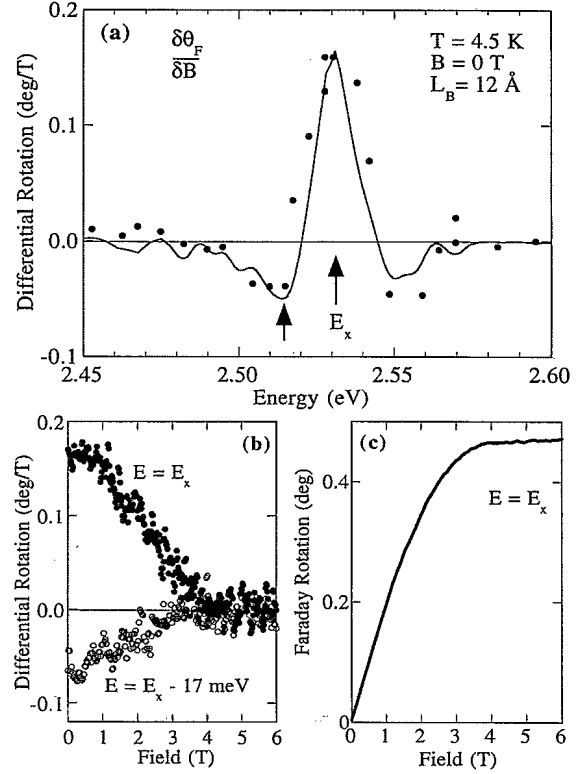


FIG. 4. (a) Differential Faraday rotation (solid circles) of the 12-Å MCDQW taken spectrally at zero field and corresponding prediction (solid line) from Kramers-Krönig analysis of the exciton absorption which is also centered at E_x . (b) DFR signal at two energies [marked by arrows in (a)] as the dc magnetic field is ramped up to $B=6 \text{ T}$. (c) The total Faraday rotation found by integrating the DFR taken at the exciton peak, showing saturation of the magnetization above 4 T.

$\partial v \Delta E_{\pm} / \hbar$, appropriate for Zeeman shifts $\Delta E_{\pm} = g_{\text{eff}} \mu_B B$ that are smaller than the linewidth. This calculation is shown by the solid line in Fig. 4(a) and adequately accounts for the observed line shape. We note that this measurement of Faraday rotation is taken across the entire vicinity of the semiconductor band gap, normally technically infeasible due to the opacity of this spectral region. Additionally we have verified the energy scaling behavior in an epilayer sample at lower energies with the form traditionally adopted.¹ The negative sidebands to the Faraday resonance arise from the difference of two dispersive refractive index line shapes corresponding to the two circular polarizations. For Zeeman shifts small compared to the linewidth, Eq. (3) produces

$$\text{DFR}(\omega) = \frac{\omega L_{\text{eff}} \mu_B g_{\text{eff}}}{2\hbar c} \frac{\partial \eta}{\partial \omega}, \quad (4)$$

where the final term controls the spectral shape and follows $\partial^2 \alpha / \partial \omega^2$.

The KK fit displayed has been arbitrarily scaled, but calculations give the rise order of magnitude for the DFR, taking into account the experimental laser bandwidth and wavelength range used. In addition, a small wavelength-independent background component to the DFR signal which does not originate from the magnetic

barriers has been subtracted out. Figure 4(b) shows the DFR recorded as the magnetic field increases with saturation apparent by $B=4$ T. The two detection energies shown correspond to the positive and negative peak amplitudes in Fig. 4(a), and are seen to behave similarly demonstrating their common origin. Because the DFR is measured continuously with magnetic field, it can be integrated directly to yield the total Faraday rotation from this 12-Å-thick magnetic alloy layer. Figure 4(c) shows θ_F at the resonant energy, and demonstrates its close relation to the magnetization, which follows a Brillouin function.¹ Adopting a Lorentzian absorption line shape (for simplicity) of oscillator strength f_{\pm} , and a half width at half maximum (HWHM) linewidth γ_{\pm} , centered at ω_{\pm} for the spin-up (−) and spin-down (+) excitons, so that the refractive indices

$$\eta_{\pm} = \text{Re}\{f_{\pm}/(\omega - \omega_{\pm} + i\gamma_{\pm})\}, \quad (5)$$

and in the limit of small shifts (so that $f_{+} \approx f_{-} = f$, $\gamma_{+} \approx \gamma_{-} = \gamma$) the peak Faraday rotation is proportional to the magnetization,

$$\theta_F^k(\omega_{\text{ex}}) = \frac{f}{(\hbar\gamma)^2} \Delta E_{\pm} = \frac{f}{(\hbar\gamma)^2} \frac{(\alpha - \beta)}{g_{\text{Mn}}\mu_B} M, \quad (6)$$

where α and β are exchange integrals for the carrier-ion interaction integrated over the electron- and hole-confined wave functions. The magnetization $M = -x_{\text{Mn}}N_0g_{\text{Mn}}\mu_B\langle S_z \rangle$ depends on the magnetic concentration x_{Mn} , the number of cations per unit volume N_0 , the magnetic-ion g factor $g_{\text{Mn}} \sim 2$, and the average z component of the spin, $\langle S_z \rangle = -S_{\text{Mn}}B_J\{g_{\text{Mn}}\mu_B S_{\text{Mn}}B/k_B T\}$, which follows a Brillouin function B_J dependent on the Zeeman energy of the $S_{\text{Mn}} = -\frac{1}{2}$ spins competing with thermal activation.

The low-field Verdet coefficient [$V = (1/L_{\text{eff}})(\partial\theta_F/\partial B)|_{B=0}$] in this structure [using Fig. 4(c) and adopting a total thickness $L_{\text{eff}} = 92$ Å] exceeds 2×10^5 deg/T cm, sufficiently large when coupled with the current experimental sensitivity to allow optical techniques to resolve magnetizations from nanoscale systems impossible to obtain using conventional superconducting quantum interference device (SQUID) magnetometry. This advantage accrues from the strong coupling of the magnetization with electronic wave functions which are tailored to restricted geometries and probed at specific energies, as compared to direct magnetic measurements which effectively integrate over all energies and the entire sample volume.

As the Zeeman splitting becomes significantly larger than the linewidth, a more complicated DFR line shape is predicted as apparent for the SSL sample in Fig. 5. The DFR measured against detection energy and magnetic field displays field tuning of the spin-up and -down transitions, as well as several other oscillatory low-field features unresolved in magnetoabsorption data. The magnitude of the DFR is ~ 100 times greater than in the MCDQW samples due to the larger g factor ($\sim \times 10$) from enhanced carrier-ion overlap, and the larger oscillator strength ($\times 10$) from the repeated structure.

These static measurements of the Faraday rotation

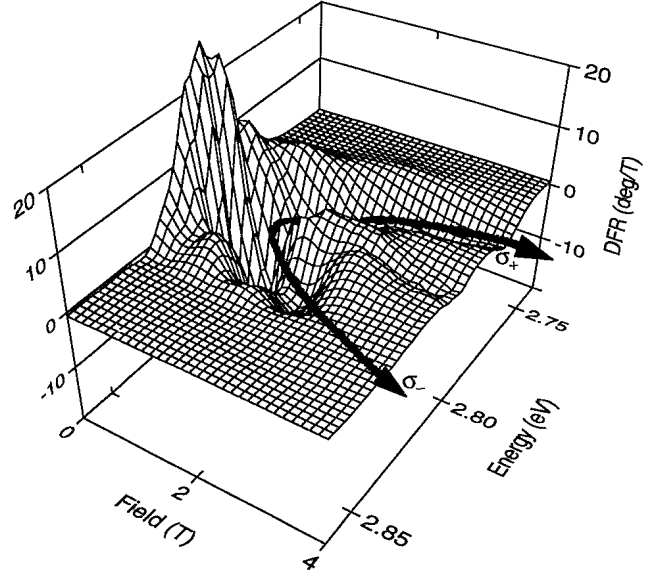


FIG. 5. Differential Faraday rotation as a function of magnetic field and photon energy for the SSL sample at $T=4.5$ K. Aside from expected spin-up (σ_-) and spin-down (σ_+) Zeeman shifts (as annotated), oscillatory low-field features near $E \sim 2.82$ eV are apparent, as well as higher-field features around $E \sim 2.80$ eV.

confirm the consistency of the technique and allow examination of ultrathin layer magnetizations in a variety of structures. The magnetic ions are verified to act paramagnetically in the nanometer alloy films and strongly influence the carrier spin energies. In Sec. IV, we examine their influence on the carrier spin dynamics by extending the Faraday rotation technique into the time domain.

IV. TIME-RESOLVED FARADAY ROTATION

A. Experimental technique

By utilizing ultrafast laser probe pulses, the Faraday rotation can be measured at some fixed time delay after a pump pulse has excited the sample (Fig. 6). The dynamics can then be mapped out by varying the interpulse time delay using a computer-controlled, scanning retroreflector. The pulses are generated in the near infrared using a passively mode-locked Ti:sapphire laser pumped by a stabilized Ar^+ laser. Over a watt of average power is obtained in 120-fs pulses, tunable from 800 nm to 1 μm , which are subsequently frequency doubled into the 400–500-nm range using a noncritically phase-matched crystal of β -barium borate ($\beta\text{-BBO}$), only 1 mm thick to preserve the temporal resolution. A dichroic mirror directs the blue light into a pulse picker which reduces the 76-MHz repetition rate of the pulse train. This LiNbO_3 acousto-optic crystal is driven by 380-MHz rf pulses (triggered synchronously from an electronically generated subharmonic of the laser output) and diffracts pulses with $\sim 30\%$ efficiency into the remainder of the experiment. The selected pulse train is divided unequally into pump and probe beams with relative intensities of

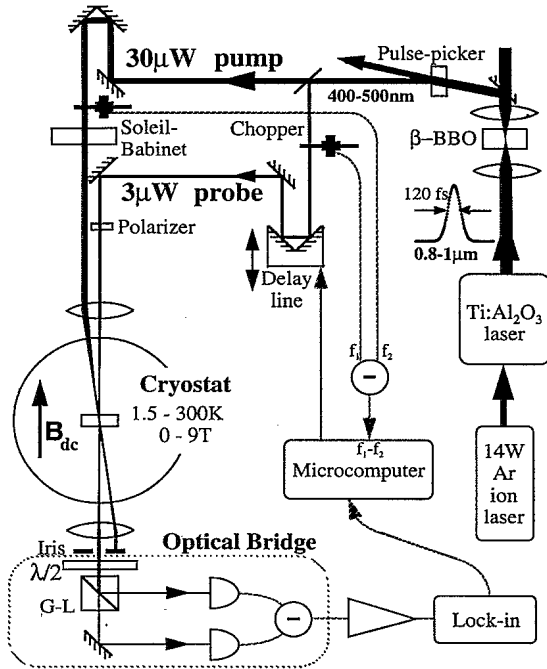


FIG. 6. Schematic apparatus for pump-probe experimental technique used to measure time-resolved Faraday rotations.

10:1, respectively, throughout all the experiments. The probe beam is focused through a mechanical chopper rotating at 1.1 kHz, linearly polarized and focused through the sample into the optical bridge. Similarly the pump beam is chopped at 400 Hz and reflected from the computer-controlled delay stage before passing through a Soleil-Babinet compensator to set its polarization. After focusing through the same 100-μm spot on the sample, it is carefully masked off to avoid saturating the balanced detectors. Circular pump polarizations were optimized at the cryostat (since mirrors in this wavelength range severely distort the polarization) and were confirmed to retain their integrity in large magnetic fields. Using phase-sensitive detection at the difference frequency of pump and probe modulations (700 Hz), the pump-induced change in probe Faraday rotation from the sample, $\Delta\theta_F(\tau)$, is recorded at each time delay τ , obviating the need for the previous coil modulation scheme (Sec. III). The signal is again normalized by simultaneously recording the probe intensity on the photodiodes. Care is taken not to include spurious pump-induced deflection or defocusing of the probe beam by adjusting the subsequent apertures in the detection system to collect all the transmitted probe and reject scattered light.

The pulse picker allows the reduction of the average power impinging on the sample while retaining the same peak powers. Figure 7 demonstrates how essential this is by showing the power dependence of the pump-induced Faraday rotation in a MCDQW sample at time delays just before ("long-lived") and just after ("initial") the pump pulse arrives. The long-lived component actually corresponds to the signal remaining from the previous pump pulse and this contaminating background clearly decreases as the time between pulses is increased, while

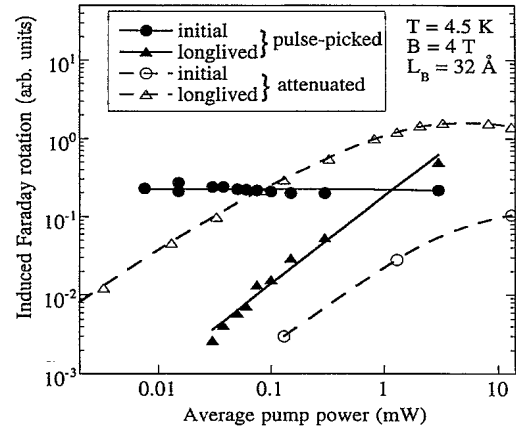


FIG. 7. Scaling behavior of the time-resolved Faraday rotation with pump intensity recorded at pump-probe time delays $\tau = +1$ ps ("initial") and $\tau = -5$ ps ("longlived"). The latter corresponds to signals remaining from the previous pump pulse at $\tau = N \times 13$ ns–5 ps, where N is the selected reduction in pulse repetition rate. The solid points ("pulse picked"), taken by changing the interpulse repetition (via N), thus employ the same peak pump power, whereas attenuating the laser intensity (open points) reduces the peak power for the same 80-MHz repetition rate.

the initial signal from each pulse remains unchanged (solid points). The long-lived signal has a decay time ~ 4 μs, and is probably caused by carrier-induced heating of the magnetic spin system as discussed below. In contrast, if the pump and probe beams are attenuated so that the pulse separation is fixed but the peak power reduced, then the long-lived background *always* dominates the time-resolved Faraday rotation invalidating the data. In these experiments, unless otherwise indicated, the interpulse separation is 650 ns and the average pump power is 30 μW which keeps the background contribution under 5% of the time-resolved signals (this offset is subtracted out of the data presented). At higher peak pump powers some saturation of the signals is evident, as the injected carrier density becomes comparable to the saturation density of the quantum well ($\sim 10^{11}$ cm⁻²). Work here concentrates on the regime several orders of magnitude below this. It is interesting to note that probing magnetically doped systems imposes stringent requirements for average optical powers to be smaller than with conventional semiconductor heterostructures due to the relaxation processes present.

B. Time-resolved spin dynamics

Femtosecond Faraday rotation data from the 32 Å MCDQW is shown in Fig. 8(a) at $T = 4.5$ K and $B = 0$ T for both circular and linear pump polarizations. The σ_+ circular polarization resonantly excites spin-down excitons and produces an ultrafast rise in the induced Faraday rotation. Interference fringes between pump and probe beams at zero delay limits the experimental resolution to 300 fs. Using the opposite circular polarization σ_- pumps spin-up excitons and gives rise to an opposite-

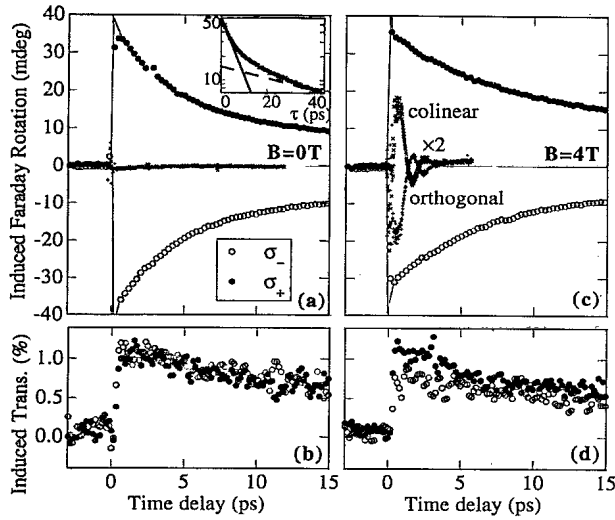


FIG. 8. (a) Pump-induced Faraday rotation data from the 32-Å sample at $T=4.5$ K, $E=E_x$, for zero field, taken using circular (σ_+ , σ_-) and linear (\parallel , \perp) pump polarizations. Inset: σ_+ pump signal on a longer time scale, showing two characteristic decay times of ~ 6 (solid line) and ~ 70 ps (dashed line). (b) Simultaneously recorded time-resolved transmission scan showing induced bleaching of the exciton absorption. (c) and (d) Corresponding data at $B=4$ T.

ly directed but otherwise identical induced Faraday rotation at zero field. The origin of this signal arises from the spin-selective bleaching of the exciton oscillator strengths by nonlinear electronic processes. As carriers are injected they prevent further absorption into the same states due to Pauli exclusion (or equivalently, phase-space filling). In addition, the carriers screen out the electron-hole binding potential of the exciton and renormalize the binding energy. All these contributions act to reduce the oscillator strength of the particular spin state which is excited, thus producing a Faraday rotation according to Eqs. (2) and (5). Hence the electronic contribution to this Faraday rotation signal comes from a pump-induced difference in oscillator strengths $\Delta(f_+ - f_-)$ arising from the net spin of the excited carriers, rather than an induced change in the Zeeman-split energies, $\Delta(\omega_+ - \omega_-)$, which stems from magnetic contributions present at nonzero field. This is verified by using a linearly polarized pump (of either orientation relative to the probe polarization) which excites equal populations of spin-up and -down carriers. No net carrier magnetization is produced and indeed no signal is seen. To confirm our interpretation, conventional pump-induced transmission changes are also recorded using the sum of the two diode photocurrents. Although this signal is noisier due to now unbalanced intensity noise contributions from the laser, both circular polarizations produce identical bleaching of the absorption simultaneously with oppositely induced Faraday rotations [Fig. 8(c)].

In contrast to observations in the magnetically coupled DQW samples, similar measurements in the SSL structures fail to elicit a significantly *spin-dependent* induced Faraday rotation. Long-lived Faraday and absorption signals are present; however, they appear to arise from

the substantial carrier density injected into the nonmagnetic ZnSe barrier material which contains most of the oscillator strength in this spectral region of the sample [Fig. 1(b)]. Because of these complications, we concentrate on time-resolved measurements of the MCDQW samples in which the excitons are spectrally distinct from the confining semiconductor layers.

After the carriers have been injected into the quantum wells, spin scattering acts to equilibrate the spin populations so that the decay of the time-resolved Faraday rotation (TRFR) provides a direct measurement of the spin-scattering time. Against expectations, the fast spin equilibration does not appear complete but ceases after ~ 10 ps, and a longer decay (~ 70 ps) of the TRFR takes over [inset, Fig. 8(a)]. This latter decay coincides with the carrier lifetime, as identified from the pump-induced absorption measurements and separately measured time-resolved photoluminescence data.⁵ All the MCDQW samples demonstrate this double exponential decay, including a nonmagnetic barrier DQW control sample, thus the cause of this behavior is not magnetic in origin. Similar dynamics have been previously identified in related experiments in GaAs;⁶ however, the introduction of magnetic ions is predicted to enhance scattering processes.⁷ At zero field there is no dc Faraday rotation, so no electronic component of the TRFR signal is expected once the spin populations have thermalized. Several possibilities would admit a nonexponential signal decay.

(a) The spin-scattering dynamics change as a function of time either through a carrier-density dependence or a localization of the carriers as they cool. However, the former is ruled out since identical behavior is obtained at 10% of the pump intensity, and the latter discounted since the shorter-lived component actually dominates at lower pump energies where the injected excitons are more localized and should exhibit less spin-flip scattering.

(b) Alternatively, two separately excited spin systems with different characteristic spin-scattering times of ~ 6 and > 70 ps would produce these observations. Models previously suggested include separate light-hole (lh), heavy-hole (hh), exciton, and electron spin-flip rates.⁸ Hole spin-flip scattering is expected to be fastest in the bulk due to hh-lh mixing away from $k=0$, but in quantum wells this is slower due to confinement- and strain-induced splitting of the hh and lh states (though possibly accelerated by the large range of k states from which the confined excitons are composed). This scheme has been used to account for spin relaxation in GaAs systems.⁹

Several features appear when a magnetic field is applied [Fig. 8(c)]. Pumping a specific spin state with circularly polarized light evokes a similar response to that at zero field, except that the symmetry between spin-up and -down is destroyed by breaking the energy-level degeneracy. Small changes in the amplitude of the initial TRFR signal may reflect slightly unequal carrier densities injected into each of the two states, because they now possess different spectral overlap with the pump pulse. For both carrier-spin orientations, the initial fast spin-flip time becomes longer, which is surprising since enhanced scattering into the energetically-favored spin-down state is expected. This suggests the fast spin-flip scattering

process is dominated by a kinetic barrier which increases with magnetic field rather than a thermodynamic balance. Further studies of this fast decay time with field (inset, Fig. 9), demonstrate that once a critical field (~ 1 T) is exceeded, no further decrease in the scattering rate is seen. To account for these two different field regimes, the scattering mechanism must be sensitive to the breaking of degeneracy by the Zeeman splitting. Such behavior is expected if fewer scattering events are then able to satisfy energy and angular momentum conservation. Below the critical field, the random orientation of uncompensated internal fields in the sample experienced by the delocalized carriers would restore many more possible scattering events. This field reflects the spatially averaged spin variance $\langle \Delta S_z^2 \rangle$ and appears to be comparable in all of our samples. It is also clear from Fig. 9 that injecting lower-energy excitons provides greater stability against spin scattering. Once they localize, excitons experience less overlap with the interface and barrier regions which seem to enhance the measured scattering rate.¹⁰

Applying magnetic fields to these nanometer-thick magnetic systems also results in the appearance of oscillations when pumping with linear polarizations, as seen previously in nonmagnetic GaAs quantum wells.¹¹ The creation of equal spin densities might be expected to produce only a small signal as carriers spin scatter predominantly into their preferred lower-energy state. Instead, strong oscillations are seen whose frequency and damping can be magnetically tuned. The beat frequency follows the Zeeman splitting of the exciton states, and the decay of their visibility corresponds to phase-scattering processes as the carriers tunnel back and forth through the magnetic barrier, destroying coherence between the excited spins. In contrast to nonmagnetic systems, we see a strong increase in the phase scattering as magnetic fields are applied. The behavior of these terahertz “spin beats”

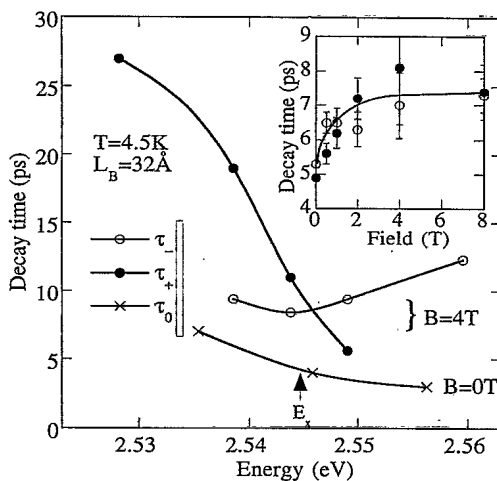


FIG. 9. Measured initial spin-scattering decay times for selected pump/detection energies around the exciton peak at zero field (τ_0) and $B=4$ T for σ_+ (τ_+) and σ_- (τ_-) pump polarizations. Inset: decay time dependence (τ_+ , τ_-) on applied field at $E=E_x$. Lines are provided as a guide to the eye.

with magnetic field and barrier thickness has been reported elsewhere,¹⁰ along with a description of their origin.

The oscillation frequency is found to be independent of pump or probe intensity and laser energy, as expected. However, as the pump energy is detuned further above the exciton peak, the oscillations lose visibility because the initial optical excitation now contains an excess of spin-up carriers (Fig. 10). Also shown (inset, Fig. 10) are several repeated scans in the immediate vicinity of the coherent artifact (used to assign zero delay) for two linear pump orientations. The artifact is considerably more pronounced for orthogonal (+) than for colinear (||) pump and probe polarizations, in contrast to conventional pump-probe spectroscopies. The photocurrent difference

$$D_{\parallel} \propto |(\mathcal{E}_{\text{pump}} + \mathcal{E}_{\text{probe}})\cos\theta_t|^2 - |(\mathcal{E}_{\text{pump}} \pm \mathcal{E}_{\text{probe}})\sin\theta_t|^2$$

(with $\theta_t \sim 45^\circ$ when balanced) subtracts out interference between pump and probe fields when they are copolarized (||).

C. Magnetic imprinting

Extending the results of Fig. 8 to longer time delays, we find that the exciton lifetime of both spin states in the DQW's is 30% shorter in the presence of a magnetic field (using time-resolved PL). However, the TRFR signal behaves entirely differently, with a spin-dependent ultra-long-lived component appearing, as seen in Fig. 11 at a variety of magnetic fields and temperatures. Such behavior is symptomatic of the effects elicited in magnetic heterostructures as compared to conventional semiconductor systems. It also demonstrates the versatility of the time-resolved Faraday rotation technique which can be used to examine the magnetic state of the system, even in

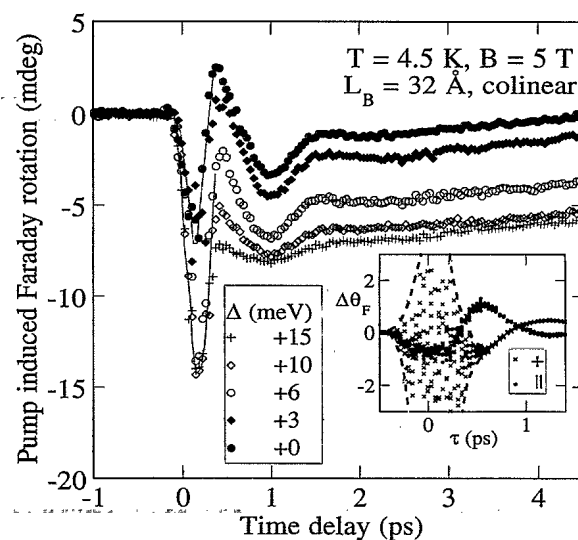


FIG. 10. Spin beating signal as a function of the detuning (Δ) of the laser from the exciton energy. Inset: Subpicosecond measurements of the induced Faraday rotation coherent artifact showing its dependence on the linear polarization of the pump. Copolarized scans (||) show suppressed interference compared to the orthogonal alignment (+).

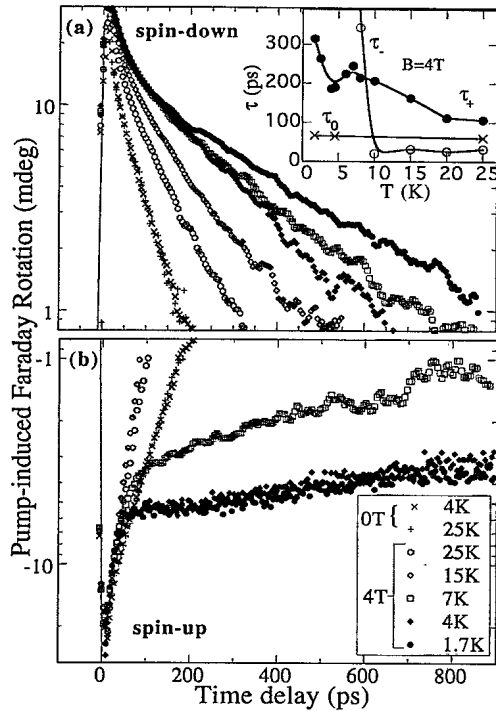


FIG. 11. Pump-induced Faraday rotation signal at long-time delays for $B=0, 4$ T and temperatures from 1.7 to 25 K on the 32-Å MCDQW sample using (a) spin-down (σ_+) and (b) spin-up (σ_-) pump excitations. Inset: Measured decay times with temperature at zero field (τ_0) and $B=4$ T for the σ_+ (τ_+) and σ_- (τ_-) pump polarizations.

the absence of any excited carriers. This complements existing optical techniques such as time-resolved luminescence which rely on carriers to radiate polarization information and have no access to long-lived magnetic signals. Optical measurement of the dynamic magnetization directly resolves the ultrafast regime and provides contrasting information to alternative physical probes such as electron-spin resonance that collect data in the spectral domain. We find the magnetization of the Mn^{2+} ions is perturbed by spin scattering with the carriers, which subsequently recombine leaving behind a magnetic “footprint.” This identification is confirmed by the lack of any corresponding signal in the 12-Å nonmagnetic-barrier control sample. The relaxation of the excited magnetic spins rapidly exceeds the maximum interpulse delay available, further demonstrating the critical need to employ pulse picking to produce meaningful results and prevent the buildup of steady-state magnetic changes.

The size and relaxation of this magnetic imprint depends on which spin orientation of carrier created it. Such behavior is unlikely to arise from thermal effects produced by the local acoustic-phonon population radiated by the cooling photoinjected carriers. Figure 11 shows that spin-up excitons create a substantially longer-lived magnetic imprint than spin-down excitons at $T=4$ K. Any explanation of these features must involve a discussion of the microscopic selection rules for spin-flip scattering of the magnetic ions by tunneling carriers, which, to our knowledge, has been impossible to examine

in any other fashion. Another immediately striking observation from the data is that the two orientations of injected spin generate magnetic relaxation with completely different thermal activations. Spin-down excitons yield an exponentially decaying signal which grows progressively slower as the temperature is reduced [inset, Fig. 11(a)], but changes little in amplitude. Spin-up excitons, on the other hand, actually provide a faster TRFR decay at $T=25$ K, but this time scale lengthens dramatically as the temperature is reduced and very rapidly exceeds many nanoseconds. The amplitude increases as the temperature drops, saturating below 4 K in concert with static magnetization data. Thus there are strong indications that more than one interaction process is needed to account for these variations. Further clues emerge from the scaling of this data with pump intensity, shown in Fig. 12. The magnetic relaxation rates at $T=4.5$ K seem remarkably unaffected by the carrier density; however, their amplitudes scale quite differently—the spin-down excitons generate a magnetic imprint whose magnitude is proportional to the pump intensity, while the corresponding scaling with spin-up excitons follows the square root of the pump power. This again suggests that more than one description is needed to account for the data, especially at low temperatures where the magnetization is saturated.

In a final comparison, data from two barrier thicknesses ($L_B=32$ and 12 Å) is compared in Fig. 13 at fields up to 8 T. As the barrier width decreases, the magnetic imprint from both spin-down and -up pumped exci-

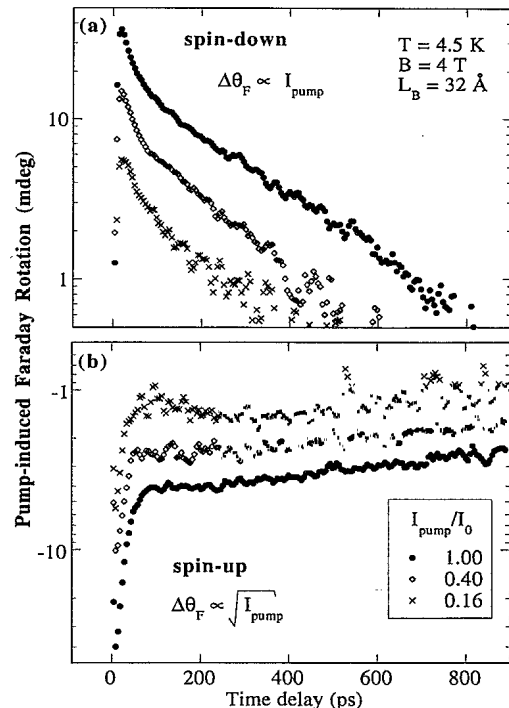


FIG. 12. Pump-induced Faraday rotations at several pump intensities display the same characteristic temporal evolution. The signal magnitude scales for (a) spin-down excitons as I_{pump} and (b) for spin-up excitons as $(I_{\text{pump}})^{0.5}$.

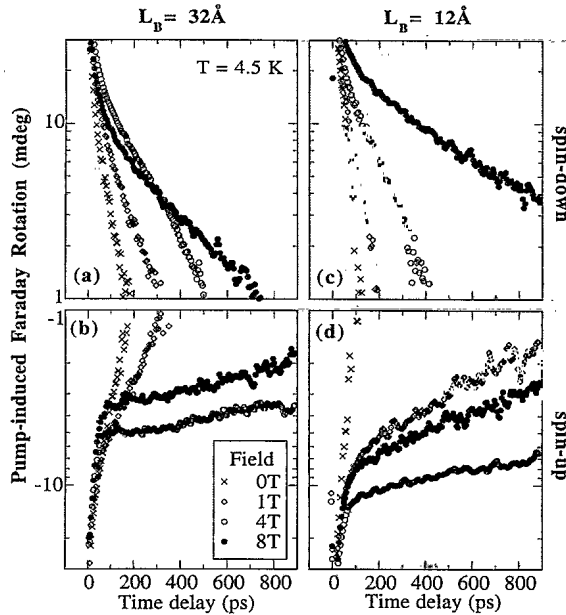


FIG. 13. Dependence of pump-induced Faraday rotation on the magnetic barrier thickness and applied magnetic field. (a) and (b) $L_B = 32 \text{ \AA}$ and (c) and (d) $L_B = 12 \text{ \AA}$. Circular pump polarization excites (a) and (c) spin-down (σ_+) excitons and (b) and (d) spin-up (σ_-) excitons.

tons increases in magnitude. In addition, the initial magnetization of the barrier determines the external field required to strongly retard magnetic relaxation.¹⁰ This is consistent with earlier static measurements, showing the magnetization to be larger in the 12-Å sample.¹²

V. DISCUSSION

These experiments access dynamic spin interactions between magnetic ions and electronic carriers for which little prior data exist. We concentrate here on understanding the spin-dependent scattering from both electronic and magnetic perspectives. In the absence of applied field, two decay times are present, the first of which is consistent with a carrier spin flip due to its rapid nature. Further support for this is postponed until we discuss the net magnetic perturbation; however, this spin flip does not appear strongly correlated with the local magnetic order. It is thus unlikely to be responsible for perturbing the magnetic system directly. On the other hand, hole spin-flip scattering may be expected to occur predominantly via the magnetic ions, since the exchange interaction is so strong (and other scattering mechanisms appear to be slower^{6,7}).

In order to provide a plausible origin for the orientation dependence of the magnetic imprints, some discussion of the microscopic scattering is pertinent. At low temperatures and large magnetic fields, most of the paramagnetic ions are oriented such that their spins are aligned against the field direction (i.e., their magnetic moments are coaligned with the field). If a spin-down carrier encounters one such ion, spin-flip scattering is suppressed since the final states could not conserve angu-

lar momentum without the presence of another particle. Conversely, an event in which a spin-up carrier ($+s_z$) is flipped to ($-s_z$), while the oriented ion ($S_z = -\frac{5}{2}$) is excited into a higher-lying Zeeman level ($S_z = -\frac{3}{2}, -\frac{1}{2}, \dots$), is comparatively favored. Because the Zeeman splitting of the individual magnetic ions is much less than that of the delocalized carriers ($g_{\text{Mn}} \ll g_{e,h}$), conservation of energy for this interaction demands that initial and final carrier states are nearly degenerate levels from each inhomogeneously broadened band of spin states (i.e., at different relative energies within each band). This implies that the nature of the carrier wave function will change at a spin flip (e.g., localizing further). Although spin-dependent selection rules might explain why different magnitudes of magnetic imprint could arise from spin-selective excitation, they cannot account for the different relaxation phenomena once the carriers have recombined.

To draw further conclusions, we note from Fig. 11 that one orientation of excitons leads to a decreased magnetization, while the opposite spin orientation leads to a contrasting *increase*. This occurs despite confirmation from static Faraday rotation measurements that show the magnetization is already saturated under these experimental conditions. We believe an understanding of the enhanced magnetization lies in the presence of strong antiferromagnetic clustering at low temperatures, a generally accepted feature of these systems.^{13,14} At Mn^{2+} concentrations above a few percent, the superexchange magnetic coupling between the ions becomes significant, leading to the formation of local antiferromagnetically oriented clusters of ions. This reduces the total magnetization of the alloy and, while remaining free spins and uncompensated clusters behave roughly paramagnetically at low fields, steps in the magnetization appear at considerably higher fields due to the internal realignment of spins within the clusters.¹⁵ Experiments here operate well below the static fields necessary to defeat antiferromagnetic clustering; however, the local exchange field from an oriented carrier passing through the structure can be extremely high, and may be sufficient to enable spin-flip scattering of this population of "spin-locked" ions.

Spin-up excitons ($S_z = -1$) consist of a spin-up electron ($s_e = +\frac{1}{2}$) and a spin-down hole ($s_h = -\frac{3}{2}$). From the previous discussion of selection rules, we would not expect this hole to undergo magnetic spin scattering as there are no free spin-up magnetic ions to participate at $B > 4 \text{ T}$, $T = 4.5 \text{ K}$. However, if we include the possibility that the hole can change the spin configuration inside a cluster, then an entirely different magnetic relaxation behavior may be expected. This would involve ion-ion interactions as well as spin-lattice mechanisms, and might be considerably slower since many magnetic spins need reorientation in the relaxation process. Such dynamics would only start to dominate when the lattice temperatures dropped below the nearest-neighbor energy $J_{\text{NN}} \sim 13 \text{ K}$, as evident for spin-up excitation in Fig. 11 [(b) and inset]. Spin-down excitons would be able to excite the paramagnetic ions from their lowest-energy states and thus decrease the net magnetization. Their magnetic recovery depends on the details of various inter-Zeeman-level Mn^{2+} transitions which control the cooling rate via

spin-lattice phonon processes, and are indeed predicted to slow down as the temperature is reduced.¹⁶ However, quantitative comparison of the scaling is unfeasible since the initial magnetic state also changes as the temperature is reduced and the population redistributes within the Zeeman-split sextuplet. The nonmonotonic temperature dependence of the relaxation time τ_+ from the spin-down magnetic imprint (inset, Fig. 11) suggests a feature close to the expected spin-glass freezing temperature of this sample ($T_g \sim 6$ K). Below this temperature, longer-range correlations between magnetic ions are significant and the size of the antiferromagnetic clusters can increase as their orientations lock together. This should be reflected in the dynamics of the magnetic relaxation, and further work is in progress to pursue such issues.

Within this phenomenological description, the number of spin-flipped magnetic ions should depend on the number of excitons injected into the quantum wells. This scaling is recovered for spin-down pumping [Fig. 12(a)]; however, the intensity dependence of the spin-up magnetic imprint is significantly different (but seen in all the magnetic barrier samples). One possible origin of such behavior would derive from the smaller number of clusters in the barrier than free spins, and their larger scattering cross section. As the carrier density increased, it would become increasingly likely for a second spin flip in the same cluster to reverse the effects of the first, thus canceling some of the effects of an increased carrier population. We were unable to acquire data at lower intensities due to the necessity of decreasing the probe power in concert with the pump power, unacceptably degrading the signal-to-noise ratio.

We note in passing the existence of higher-energy, optically accessible, excited states of the manganese ions which lie ~ 2 eV above the d subband.¹⁷ Luminescence from these levels is particularly noticeable from the heavily doped epilayer samples and has a long lifetime ($> 20 \mu\text{s}$) uncorrelated with that of the carriers. It is possible that these Mn^{2+} levels also play a role in the magnetic relaxation; however, their energy is not field sensitive and the process by which they acquire energy from the carriers is currently unclear.

VI. CONCLUSION

In summary, we reemphasize the utility of femtosecond-resolved Faraday rotation in studying the spin dynamics of both photoinjected carriers and the magnetic system of ions with which they interact. Partnering this technique is the fabrication of spin-engineered magnetic heterostructures that offer a well-controlled environment in which to probe spin interactions in detail. We have presented highly sensitive static

Faraday rotation measurements on films as thin as three monolayers with 24% magnetic cation concentration in order to characterize their magnetic state. Such measurements are beyond the current limits of dc SQUID technology, and exemplify the benefits of using spectroscopic methods with semiconductor materials.

Many physical processes can be identified using this ultrafast probe which captures both the average carrier magnetization (net electronic spin) and the instantaneous cation magnetization (net magnetic spin). Spin-selective excitation of excitons using circularly polarized light immediately bleaches the relevant spin states (within 300 fs). The subsequent decay of this signal resolves a ~ 6 -ps spin scattering process which slows when a magnetic field is applied. Simultaneous and coherent excitation of both exciton spin states leads to magnetically tunable terahertz oscillations in the transmitted probe polarization. Phase-scattering rates of a few picoseconds can be identified from the damping of these spin beats. Additional slow spin equilibration (> 70 ps) takes place as the excitons recombine, via spin-flip scattering of a separate population tentatively identified as heavy holes. The carrier spin cooling transfers spin excitations into the magnetic subsystem in a manner critically dependent on the exciton orientation. Spin-down carriers are suggested to carry sufficient exchange field to overcome ion-ion antiferromagnetic correlations and break apart spin-locked clusters. Spin-up carriers transiently reduce the magnetization by flipping individual, initially field-aligned, magnetic ions. The relaxation of the induced magnetic imprint depends on the parent magnetic state and how it is perturbed. For spin-down excitons, or at higher temperatures, magnetic relaxation is controlled by isolated paramagnetic ions undergoing spin-lattice interactions, whereas at low temperature the dominant slow response arises from strongly coupled antiferromagnetic clusters readjusting internally and with the lattice.

Such information about interacting spin systems should lead to a clearer understanding of the microscopic scattering processes at work in quantum geometries. Observations here detail a wealth of unexpected dynamical phenomena in both the electronic and magnetic spin systems. Each of these is excited and relaxes in an entirely different fashion, demonstrating the unique properties of magnetic semiconductor heterostructures.

ACKNOWLEDGMENTS

We are grateful to David Tulchinsky for making results available. J.J.B. would like to thank the support of IBM and Jesus College, Oxford. This work was supported by Grant Nos. NSF DMR-92-07567, NSF DMR-92-08400, and AFOSR F49620-93-1-0117.

¹*Diluted Magnetic Semiconductors*, edited by J. K. Furdyna and J. Kossut (Academic, San Diego, 1988), Vol. 25.

²D. D. Awschalom, J. F. Smyth, N. Samarth, H. Luo, and J. K. Furdyna, *J. Lumin.* **52**, 165 (1992).

³H. Luo, N. Dai, F. C. Zhang, and N. Samarth, *Phys. Rev. Lett.* **70**, 1307 (1993).

⁴J. J. Baumberg, D. D. Awschalom, and N. Samarth, *J. Appl. Phys.* **75**, 6199 (1994).

- ⁵D. A. Tulchinsky, J. J. Baumberg, D. D. Awschalom, N. Samarth, H. Luo, and J. K. Furdyna (unpublished).
- ⁶S. Bar-Ad and I. Bar-Joseph, Phys. Rev. Lett. **68**, 349 (1992).
- ⁷R. Ferreira and G. Bastard, Phys. Rev. B **40**, 1074 (1989).
- ⁸M. Z. Maialle, E. A. de Andrada e Silva, and L. J. Sham, Phys. Rev. B **47**, 15 776 (1993).
- ⁹M. Z. Maialle and L. J. Sham, in *Proceedings of the Ninth International Conference on Electronic Properties of Two-Dimensional Systems* [Surf. Sci. (to be published)].
- ¹⁰J. J. Baumberg, D. D. Awschalom, N. Samarth, H. Luo, and J. K. Furdyna, Phys. Rev. Lett. **72**, 717 (1994).
- ¹¹S. Bar-Ad and I. Bar-Joseph, Phys. Rev. Lett. **66**, 2491 (1991).
- ¹²J. F. Smyth, D. D. Awschalom, N. Samarth, H. Luo, and J. K. Furdyna, Phys. Rev. B **46**, 4340 (1992).
- ¹³J. K. Furdyna, J. Appl. Phys. **64**, R29 (1988).
- ¹⁴O. Goede and W. Heimbrodt, Phys. Status Solidi B **146**, 11 (1988).
- ¹⁵R. L. Aggarwal, S. N. Jasperson, P. Becla, and J. K. Furdyna, Phys. Rev. B **34**, 5894 (1986).
- ¹⁶M. Blume and R. Orbach, Phys. Rev. **127**, 1587 (1962).
- ¹⁷Y. R. Lee, A. K. Ramdas, and R. L. Aggarwal, Phys. Rev. B **33**, 7383 (1986).